

Comparative Dielectric Response in CaTiO_3 and $\text{CaAl}_{1/2}\text{Nb}_{1/2}\text{O}_3$ from First PrinciplesEric Cockayne¹¹*Ceramics Division, Materials Science and Engineering Laboratory,
National Institute of Standards and Technology Gaithersburg, MD 20899-8520*

CaTiO_3 (CT) and $\text{CaAl}_{1/2}\text{Nb}_{1/2}\text{O}_3$ (CAN) have similar structures but very different dielectric properties. For CT at room temperature, the relative permittivity $\kappa \approx 170$ and the temperature coefficient of resonance frequency $\tau_f \approx +900 \times 10^{-6} \text{ K}^{-1}$, but for CAN, $\kappa \approx 27$; $\tau_f \approx -88 \times 10^{-6} \text{ K}^{-1}$. We use first-principles density functional theory calculations to investigate the origin of the divergent behaviors. We find important differences between the two systems in both the frequencies and the eigenvectors of the low-frequency polar phonons. In CT, the frequencies are lower and the perovskite B site cations move against the surrounding oxygen octahedra; whereas in CAN, the frequencies are higher and the B site cations move with the oxygen octahedra. These two factors are equally important in explaining the differences in κ . We introduce and solve a decoupled quantum oscillator model for the temperature-dependent permittivity. This model predicts a large positive τ_f for CT and a small τ_f for CAN, in qualitative agreement with experiment. We relate the different dielectric behaviors to differences in the electronic structures.

PACS numbers:

I. INTRODUCTION

Dielectric materials for microwave applications must have high permittivity, low loss, and temperature stability. Uncovering the relationship between chemistry, structure, and dielectric properties is of the utmost importance for the rational design of new dielectric materials.

Some empirical structure-property relationships have been found for permittivity and temperature coefficient. Shannon[1] has found that the permittivities of a wide variety of oxides can be fit assuming additive atomic polarizabilities. These rules, however, have only been shown to work well for materials with relative permittivities $\kappa < 15$ [1], which excludes the high-permittivity materials of interest for microwave applications. Furthermore, this approach involves some unphysical assumptions, such as using the microscopic Clausius-Mossotti relationship for structures where not all ions sit on positions of cubic symmetry.

The temperature coefficient of resonance frequency τ_f of a resonator is given by

$$\tau_f \equiv \frac{1}{f} \frac{\partial f}{\partial T} = -\alpha - \frac{1}{2} \frac{1}{\kappa} \frac{\partial \kappa}{\partial T} = -\alpha - \frac{\tau_\kappa}{2}, \quad (\text{I.1})$$

where f is the resonant frequency, α the linear coefficient of thermal expansion, and τ_κ the temperature coefficient of permittivity. Much recent work has focused on the empirical correlation of τ_f (τ_κ) with the tolerance factor in perovskite-related materials[2–6]. The tolerance factor t is given by

$$t = \frac{R_A + R_O}{\sqrt{2}(R_B + R_O)}, \quad (\text{I.2})$$

where R_A , R_B , and R_O are the ionic radii of the perovskite A site cation, the perovskite B site cation, and oxygen. It has been found that smaller t correlates with more negative τ_f in a variety of systems. Here too, the relationship between tolerance factor and τ_f is not universal. For example, CaZrO_3 has a smaller t but a more positive τ_f than SrZrO_3 , although the structures differ only by isovalent substitution and are related to the undistorted perovskite structure by the same category of oxygen octahedral tilting[4]. Present empirical knowledge of structure-property relationships is thus not sufficient to reliably predict the properties of new dielectric materials.

The contrasting dielectric properties of the closely related materials CaTiO_3 (CT) and $\text{CaAl}_{1/2}\text{Nb}_{1/2}\text{O}_3$ (CAN) highlight the need for more fundamental studies of structure-property relationships. CT is a simple perovskite; CAN is a doubled perovskite with a rocksalt-like 1:1 ordering of Al and Nb on the B-site sublattice. CT and CAN have nearly identical lattice parameters, tolerance factors, and octahedral tilting patterns and magnitudes[7]. Experimentally, however, CT has $\kappa \approx 170$ [4, 8, 9] and $\tau_f \approx +900 \times 10^{-6} \text{ K}^{-1}$ at room temperature[4, 10], whereas CAN has $\kappa \approx 27$ and $\tau_f \approx -88 \times 10^{-6} \text{ K}^{-1}$ [11, 12]. Furthermore, the CT-CAN system is of experimental interest because it forms a solid solution series across the entire composition range and thus contains a single-phase material with $\tau_f = 0$, which is potentially a useful microwave dielectric material.

In order to understand the structure-property relationships that lead the simple perovskite CT to have higher permittivity and τ_f more positive and much larger in magnitude than the double perovskite CAN, we turn to first principles calculations. In a previous work[13], we used first-principles methods to successfully compute the

permittivity of CaTiO_3 via computation of its phonon properties. In this work, we apply the same method to $\text{CaAl}_{1/2}\text{Nb}_{1/2}\text{O}_3$. Then we take a step toward an understanding of the microscopic origin of τ_f by computing the intramode phonon anharmonicities to lowest order and introducing a decoupled anharmonic quantum oscillator model. We find that the same phonon characteristics that give CaTiO_3 a higher permittivity are responsible for its more positive τ_f .

II. PERMITTIVITY

By definition, the static relative permittivity tensor $\vec{\kappa}$ of a solid is given by

$$\kappa_{\alpha\beta} = \delta_{\alpha\beta} + \frac{1}{\epsilon_0} \frac{\partial P_\alpha}{\partial E_\beta}, \quad (\text{II.1})$$

where \mathbf{P} is the polarization, \mathbf{E} the applied electric field, $\delta_{\alpha\beta}$ the Kronecker delta function, and ϵ_0 the permittivity of free space.

Dispersion theory[14] shows that the permittivity tensor for a crystal within the harmonic approximation is given equivalently by[13, 15]:

$$\kappa_{\alpha\beta} = (\kappa_\infty)_{\alpha\beta} + \sum_\mu \frac{\overline{Z}^*_{\mu\alpha} \overline{Z}^*_{\mu\beta}}{V \epsilon_0 m_0 \omega_\mu^2}, \quad (\text{II.2})$$

where $\vec{\kappa}_\infty$ is the electronic dielectric tensor, μ labels the zone-center ($\mathbf{q} = 0$) infrared-active normal modes of the system, ω_μ their (angular) frequencies, $\overline{Z}^*_{\mu\alpha}$ their effective charges in Cartesian direction α , and V the volume per unit cell. The mode effective charge in the α direction for a given mode μ is defined as

$$(\overline{Z}^*_\mu)_\alpha \equiv \sum_{i\gamma} Z^*_{i\alpha\gamma} (m_0/m_i)^{1/2} (a_\mu)_{i\gamma}, \quad (\text{II.3})$$

where \vec{Z}^*_i is the Born effective charge tensor for ion i , m_i its mass, $(a_\mu)_{i\gamma}$ the component of the normalized dynamical matrix eigenvector for mode μ involving ion i in the γ direction, and m_0 an arbitrary mass, which is cancelled by the denominator of (II.2). We use $m_0 = 1$ amu in this work.

We define an “ideal ceramic” as one whose physical properties are simply the average of the constituent material over all orientations. The dielectric constant of an ideal ceramic is

$$\kappa = \frac{1}{3} \text{Tr}\{\vec{\kappa}\} \quad (\text{II.4})$$

The dispersion formula for an ideal ceramic becomes

$$\kappa = \kappa_\infty + \sum_\mu \frac{1}{3} \frac{\overline{Z}^*_{\mu\mu}^2}{V \epsilon_0 m_0 \omega_\mu^2}, \quad (\text{II.5})$$

where $\overline{Z}^*_{\mu\mu}^2 = \sum_\alpha \overline{Z}^*_{\mu\alpha}^2$.

In order to investigate the temperature dependence of κ and thus τ_f , it is necessary to go beyond the harmonic approximation. We begin with a proper quantum statistical mechanics treatment. At a given temperature, the lattice dynamics problem is a coupled anharmonic oscillator problem whose parameters are determined by an expansion of the total energy in the normal mode coordinates of the equilibrium cell. The equilibrium cell at a given temperature, in turn, is determined by the anharmonic lattice dynamics in a self-consistent manner.

Assume that one can determine the complete set of phonon eigenstates n and eigenenergies E_n for the case of a weak electric field along direction β . The quantum mechanical density operator at thermal equilibrium is diagonal with element $\rho_{nn} = \exp(-E_n/kT)/Z$, where Z is the partition function. The expectation value of the polarization along direction α is

$$\langle P_\alpha \rangle = \text{Tr}\{\rho P_\alpha\} = \sum_n \exp(-E_n/kT) \langle P_\alpha \rangle_n / Z, \quad (\text{II.6})$$

where $\langle P_\alpha \rangle_n$ is the expectation value of P_α for eigenstate n . If the material is nonpolar when the ions are in their equilibrium positions, as is the case for CT and CAN, then $\kappa_{\alpha\beta}$ is given by

$$\kappa_{\alpha\beta} = \delta_{\alpha\beta} + \frac{1}{\epsilon_0} (\lim_{|\mathbf{E}| \rightarrow 0} \langle P_\alpha \rangle_{\mathbf{E}=\mathbf{E}\hat{\beta}}). \quad (\text{II.7})$$

In Section V, we make further approximations in order to obtain a solvable model for κ as a function of temperature and thus τ_f .

III. FIRST-PRINCIPLES CALCULATIONS

All calculations are performed using VASP (the Vienna ab initio simulation package[16–19]). VASP is a code for plane-wave pseudopotential density functional theory calculations. We used ultrasoft Vanderbilt-type pseudopotentials[20] as supplied by G. Kresse and J. Hafner[21]. The total number of valence electrons used was 8 for Ca, 10 for Ti, 3 for Al, 11 for Nb, and 6 for oxygen. All of our calculations were done using the VASP high precision option, *i.e.* a plane-wave energy cutoff of 494.6 eV. We used the local density approximation (LDA) for the exchange-correlation energy. Brillouin zone integration was obtained by calculating Kohn-Sham wavefunctions for a set of 128 \mathbf{k} points in the Brillouin zone, positioned so as to be equivalent to an $8 \times 8 \times 8$ Monkhorst-Pack grid for a primitive perovskite cell.

IV. RESULTS

A Structure

Generally, LDA calculations result in a unit cell that is too small. On the other hand, physical properties calculated under the LDA have generally been found to agree better with experiment if the cell parameters are fixed at the experimental ones[22]. Since we are interested in dielectric properties, we use the experimental lattice parameters for CT and CAN here. For CT, we use the weighted average of the four structure refinements tabulated in Ref. [23]. For CAN, we use the parameters measured by Vanderah et al.[12, 24]. In each case, we started with the ions in their experimental positions and then relaxed the ions within the LDA until a total energy convergence of better than 10^{-6} eV per formula unit was obtained. The results are shown in Table I. We treat CAN as fully ordered; experimentally, occupation factors of 0.93 have been obtained[7].

TABLE I: Comparative relaxed LDA structures for CaTiO_3 and $\text{CaAl}_{1/2}\text{Nb}_{1/2}\text{O}_3$. Lattice parameters are from experiment. Space group: CT: Pbnm (#62, setting *cab*); CAN: $\text{P}12_1/\text{n}1$ (#14, unique axis *b*, cell choice 2). *a*, *b*, *c* in Å.

	CT	CAN		CT	CAN
a	5.3804	5.3773	Nb		
b	5.4422	5.4153	<i>x</i>		1/2
c	7.6417	7.6262	<i>y</i>		0
β	90°	89.97°	<i>z</i>		0
Ca			O(1)		
<i>x</i>	0.9903	0.9913	<i>x</i>	0.0807	0.0780
<i>y</i>	0.0443	0.0406	<i>y</i>	0.4783	0.4802
<i>z</i>	1/4	0.2482	<i>z</i>	1/4	0.2437
Ti			O(2)		
<i>x</i>	0		<i>x</i>	0.7093	0.7173
<i>y</i>	1/2		<i>y</i>	0.2904	0.2947
<i>z</i>	0		<i>z</i>	0.0427	0.0416
Al			O(3)		
<i>x</i>		0	<i>x</i>	(0.7907)	0.7961
<i>y</i>		1/2	<i>y</i>	(0.7904)	0.7831
<i>z</i>		0	<i>z</i>	(0.0427)	0.0405

The theoretical structures for CAN and CT are very similar. Both have the $a^-a^-c^+$ octahedral tilting pattern and all positional parameters agree to within 0.01 lattice parameters (see Figure 1).

B Born effective charges

As described in[13], we used the King-Smith and Vanderbilt[25] method to calculate the polarizations of appropriately perturbed cells and from this, the Born effective charge tensors of the ions. Full details and results for CT are given in [13]. In Table II, we give the principal

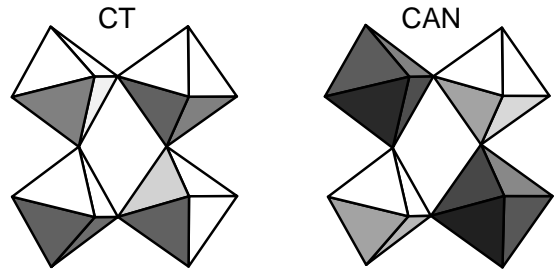


FIG. 1: Comparison of relaxed LDA octahedral tilting patterns in CT and CAN (to scale).

components of the Born effective charges, obtained by diagonalizing the tensors for each ion in CAN, and compare the results with those for CT. The nominal ionic charges of Ca, Ti, Al, Nb, and O are, respectively, 2, 4, 3, 5 and -2 . The dynamical effective charges are generally larger in magnitude than the nominal charges, especially for the B site cations and for O in the direction of the B-O bonds. The anomalies are larger in CT than in CAN. The effective Nb charge in CAN is significantly lower than that for Nb in simple ANbO_3 perovskites where it is about $+9$ [26, 27]. A similar reduction of the Nb effective charge has been observed in other complex perovskites containing Nb[28].

TABLE II: Principal components of Born effective charge tensors of for CT and CAN. (in $|e|$)

	CT	CAN		CT	CAN
$Z_{Ca,1}^*$	2.59	2.62	$Z_{01,1}^*$	-5.37	-3.81
$Z_{Ca,2}^*$	2.38	2.36*	$Z_{01,2}^*$	-2.05	-1.98
$Z_{Ca,3}^*$	2.27	2.36*	$Z_{01,3}^*$	-1.91	-1.79
$Z_{Ti/Al,1}^*$	7.06	4.06	$Z_{02,1}^*$	-5.38	-3.87
$Z_{Ti/Al,2}^*$	6.90*	3.98*	$Z_{02,2}^*$	-2.02	-1.83*
$Z_{Ti/Al,3}^*$	6.90*	3.98*	$Z_{02,3}^*$	-1.91	-1.83*
$Z_{Ti/Nb,1}^*$	(7.06)	6.26	$Z_{03,1}^*$	(-5.38)	-3.79
$Z_{Ti/Nb,2}^*$	(6.90*)	6.23*	$Z_{03,2}^*$	(-2.02)	-1.89*
$Z_{Ti/Nb,3}^*$	(6.90)	6.23*	$Z_{03,3}^*$	(-1.91)	-1.89*

*Modulus of

complex eigenvalue

C Electronic dielectric tensor

To calculate the electronic contribution to the dielectric tensors, we used a modification of the method of Bernardini, Fiorentini, and Vanderbilt[29, 30]. Full details are given in [13]. In contrast to our previous work, where we used the energy of semicore states to determine the local potential and thus the local macroscopic field, here we used the VASP option which determines the potential at the ionic centers. We weighted each ion equally; the difference in potentials between pairs of like ions at a given separation depended on the species and varied as much as $\pm 10\%$; thus the uncertainty in the electronic

dielectric constant is several percent.

The results for the on-diagonal electronic dielectric tensor components for CT and CAN are shown in Table III, along with the value $\kappa_\infty = \frac{1}{3}Tr\{\vec{\kappa}\}$ expected for an ideal ceramic. κ_∞ is about 20% larger in CT than in CAN. Unlike CT, CAN has monoclinic symmetry and thus a nonzero $(\kappa_\infty)_{xz}$. Because $(\kappa_\infty)_{xz}$ does not affect $Tr\{\vec{\kappa}\}$, we did not calculate it here.

TABLE III: Diagonal components of first-principles electronic dielectric tensors for CT and CAN.

	CT	CAN
$(\kappa_\infty)_{xx}$	6.03	4.87
$(\kappa_\infty)_{yy}$	6.02	5.02
$(\kappa_\infty)_{zz}$	6.19	4.89
κ_∞	6.08	4.93

D Phonons and Permittivity

After calculating the residual Hellmann-Feynman forces on each structure in Table I, we displaced each symmetry-independent ion in each Cartesian direction in turn by ± 0.01 Å and recalculated the forces. From finite differences, we determined the force constants matrices. We diagonalized the corresponding dynamical matrices to obtain the normal mode frequencies and eigenvectors.

The infrared phonon frequencies and symmetry labels for CT are shown in Table IV and those for CAN in Table V. We also computed the zone-center normal mode frequencies and symmetry properties for CAN in the undistorted[31] $Fm3m$ double perovskite structure at the experimental volume ($a = 2 \times 3.815$ Å) (Table VI). As was the case for CT[13], the most unstable mode found is that of out-of-phase oxygen octahedral tilting (in CT, this is a mode with $\mathbf{q} = (1/2, 1/2, 1/2)$; because of the ordering in CAN, this mode is now at the zone center). All other things being equal, we thus expect similar ferroelastic phase transitions in the two materials, with the transitions shifted to lower temperatures in CAN. There is also one unstable polar triplet in each case, though ν is shifted to higher (less unstable) frequency in CAN compared to CT. In both cases, octahedral tilting acts to suppress this ferroelectric instability which would otherwise be present.

For completeness, we report the 24 Raman active mode frequencies for CAN in Table VII. By comparing the eigenvectors of the Raman-active modes in distorted CAN with those of the 9 Raman-active modes of undistorted CAN (symmetries A_{1g} , E_g , and F_{2g}), we find that 9 modes of CAN can be associated with those of the undistorted case. To the extent that the deviation from cubic symmetry is small, we expect these peaks to have high intensity and the others to be weaker. The predicted Raman peak at 797 cm^{-1} is due to symmetric breathing,

TABLE IV: First-principles phonon symmetry labels, frequencies ν (in cm^{-1}), effective charges \bar{Z}^* (in $|e|$), quartic potential term B (in 10^{18} J/m⁴), harmonic contributions to dielectric permittivity κ_{ha} , contributions to dielectric permittivity in decoupled anharmonic quantum oscillator model κ_{qu} at zero temperature and room temperature (RT) = 25°C , and contribution to τ_f at RT (in 10^{-6} K⁻¹) for polar modes in CaTiO₃. Electronic contribution to, and total dielectric constant are shown, assuming κ_∞ to be temperature-independent.

label	ν	\bar{Z}^*	B	κ_{ha}	κ_{qu} (0 K)	κ_{qu} (RT)	τ_f (RT)
B_{1u}	87	2.84	16.15	78.64	49.23	33.42	+129
	112	1.31	6.27	10.03	8.82	7.32	+16
	171	1.19	2.35	3.53	3.47	3.40	+1
	251	0.39	3.71	0.18	0.18	0.17	0
	423	0.74	1.09	0.22	0.22	0.22	0
	468	0.04	11.18	0.00	0.00	0.00	0
	508	1.36	11.26	0.52	0.52	0.52	0
B_{2u}	103	3.10	13.94	65.77	49.46	37.18	+117
	161	1.29	1.12	4.66	4.62	4.55	+1
	217	0.38	0.97	0.23	0.23	0.23	0
	250	0.55	1.27	0.36	0.36	0.36	0
	294	0.75	0.86	0.48	0.48	0.47	0
	332	0.18	4.19	0.02	0.02	0.02	0
	480	0.47	1.01	0.07	0.07	0.07	0
	505	1.20	3.93	0.42	0.42	0.42	0
	546	0.12	-0.22	0.00	0.00	0.00	0
	547	0.12	-0.22	0.00	0.00	0.00	0
B_{3u}	85	3.15	15.70	99.48	62.59	42.47	+163
	160	0.94	0.61	2.52	2.51	2.49	0
	199	0.50	1.13	0.46	0.46	0.45	0
	271	0.01	3.09	0.00	0.00	0.00	0
	311	0.64	1.66	0.31	0.31	0.31	0
	362	0.29	1.15	0.05	0.05	0.05	0
	424	0.80	3.53	0.26	0.26	0.26	0
	483	0.04	-0.28	0.00	0.00	0.00	0
	525	1.24	7.44	0.41	0.41	0.41	0
κ_∞				6.08	6.08	6.08	
$(\kappa)_{total}$				274.70	190.75	140.87	
$(\tau_f)_{total}$							+428

the split doublet at $553\text{--}554$ cm^{-1} is due to asymmetric breathing, and the split triplets at $446\text{--}457$ cm^{-1} and $188\text{--}242$ cm^{-1} are due to Ca motion and O motion transverse to Al-O-Nb bonds. For the $188\text{--}242$ cm^{-1} modes, the amplitude of Ca motion is largest, for the $446\text{--}457$ cm^{-1} modes, the amplitude of the O motion is largest.

The magnitudes of the mode effective charges, as defined in Eq. (II.3), are given for each infrared active (polar) mode in Tables IV-V and Figure 2. The harmonic contribution of each infrared active mode to the static dielectric constant is given in Tables IV-V and Figure 3, using Eq. (II.2) with $\omega_\mu = 2\pi c\nu_\mu$, where ν_μ are in cm^{-1} and c is the speed of light. The total static dielectric tensor in the harmonic approximation, obtained by summing up the mode contributions and the electronic dielectric tensor, is given in Tables IV-V.

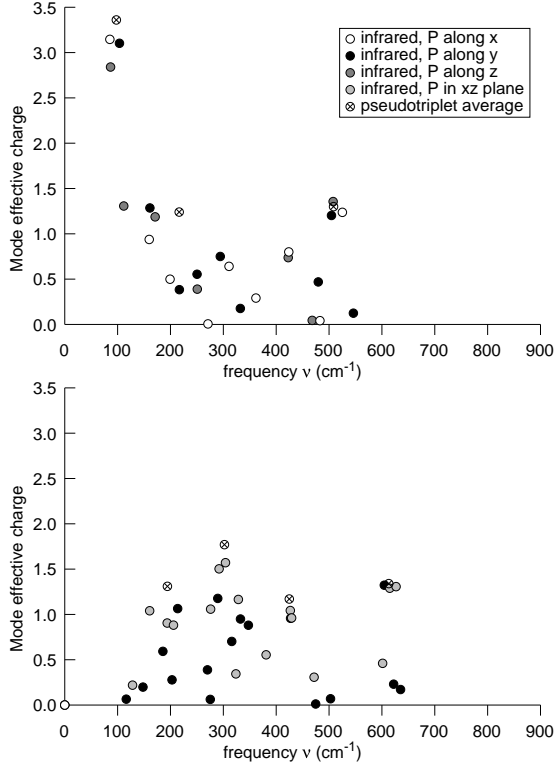


FIG. 2: Mode effective charges of polar modes in CT and CAN

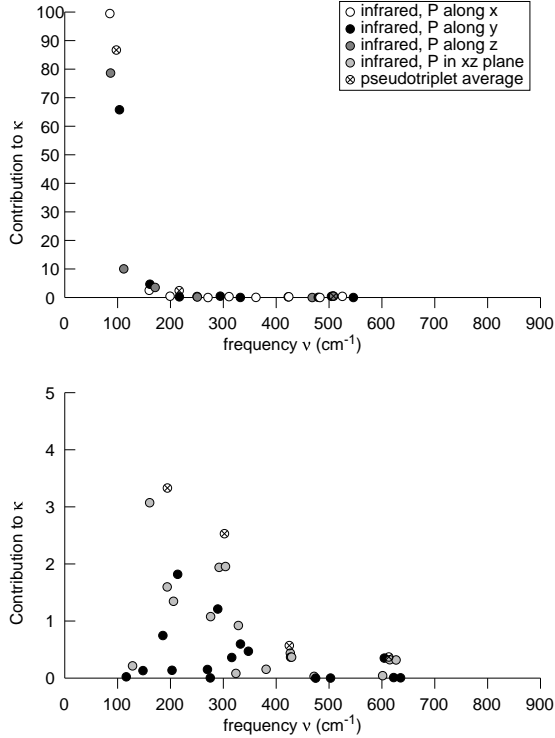


FIG. 3: Mode-by-mode contributions to total dielectric constant of CT and CAN within harmonic approximation.

TABLE V: Same as Table IV, for CAN.

label	ν	\bar{Z}^*	B	κ_{ha}	κ_{qu} (0 K)	κ_{qu} (RT)	τ_f (RT)
A_u	116	0.07	0.26	0.02	0.02	0.02	0
	148	0.20	0.20	0.13	0.13	0.13	0
	186	0.59	1.21	0.75	0.75	0.74	+1
	203	0.28	0.43	0.14	0.14	0.14	0
	214	1.06	1.60	1.83	1.82	1.81	+1
	270	0.39	1.32	0.15	0.15	0.15	0
	275	0.06	1.24	0.00	0.00	0.00	0
	289	1.57	1.34	1.22	1.22	1.22	0
	316	0.70	3.04	0.36	0.36	0.36	0
	332	0.95	4.00	0.60	0.60	0.60	0
	347	0.88	3.64	0.47	0.47	0.47	0
	427	0.96	8.48	0.37	0.37	0.37	0
	475	0.01	2.47	0.00	0.00	0.00	0
	503	0.07	25.86	0.00	0.00	0.00	0
	604	1.32	18.82	0.35	0.35	0.35	0
	622	0.23	15.45	0.01	0.01	0.01	0
	635	0.17	18.31	0.01	0.01	0.01	0
B_u	128	0.22	0.24	0.22	0.22	0.21	0
	161	1.04	1.70	3.10	3.05	2.99	+6
	194	0.90	0.78	1.60	1.60	1.59	+1
	206	0.88	0.90	1.36	1.35	1.35	+1
	276	1.06	2.80	1.09	1.08	1.08	0
	292	1.50	0.81	1.95	1.95	1.95	0
	304	1.57	2.83	1.97	1.96	1.96	+1
	324	0.34	1.68	0.08	0.08	0.08	0
	328	1.17	3.38	0.93	0.93	0.92	0
	381	0.55	2.31	0.16	0.16	0.16	0
	427	1.04	7.60	0.44	0.44	0.44	0
	429	0.96	3.35	0.37	0.37	0.37	0
	472	0.31	5.21	0.03	0.03	0.03	0
	601	0.46	17.66	0.04	0.04	0.04	0
	615	1.29	29.31	0.32	0.32	0.32	0
	627	1.31	19.76	0.32	0.32	0.32	0
κ_∞				4.93	4.93	4.93	
$(\kappa)_{total}$				25.34	25.24	25.13	
$(\tau_f)_{total}$							+11

In Figures 2-3, pseudotriplet averages are shown. An undistorted simple perovskite has three infrared-active triplets; while an $Fm3m$ ordered double perovskite has four infrared-active triplets. In the case of CT and CAN, the low-temperature phases are distorted from cubic symmetry due to octahedral tilting. If the distortion of the structure from cubic symmetry is small, the cubic triplets will evolve to pseudotriplets, while new, low \bar{Z}^* infrared active modes will appear. If the distortion from cubic symmetry is large, one can nonetheless still define “pseudotriplets” by the following method: Let n_u be the number of zone-center polar triplets for the cubic phase ($n_u = 3$ for CT and 4 for CAN). Let $\{e_{\lambda\alpha}\}$ be the eigenvectors for the the polar zone-center triplets of the ideal perovskite structure with polarization in Cartesian direction α , and $\{e_\mu\}$ the eigenvectors of the polar modes of the distorted structure, μ arranged in order of increasing

TABLE VI: Frequencies (in cm^{-1}) for optical zone-center modes for ordered CAN in the undistorted $Fm3m$ double perovskite structure with $a = 2 \times 3.815$ Å. Phonons are grouped by irreducible representation. F_{1u} frequencies are for transverse optical modes. Imaginary frequencies indicate harmonic instabilities.

Label	ν	Label	ν	Label	ν
A_{1g}	911	F_{1u}	48 i	F_{2g}	102
E_g	660	F_{1u}	304	F_{2g}	445
F_{1g}	208 i	F_{1u}	487	F_{2u}	204
		F_{1u}	733		

TABLE VII: Computed frequencies of Raman-active modes in CAN (in cm^{-1}). Starred frequencies are those for modes whose eigenvectors most closely correspond to those of the nine Raman-active modes for an undistorted ordered CAN perovskite.

Label	ν					
A_g	136	162	188*	242*	289	331
	339	452*	457*	553*	564	797*
B_g	175	182	185	211*	237	351
	359	446*	482	554*	732	770

ν_μ .

Each mode μ of the distorted structure gets a weight $C_{\mu\alpha}$ for each direction α according to the total squared projection of its eigenvector onto the α eigenvectors of the undistorted structure: $C_{\mu\alpha} = \sum_{\lambda=1}^{n_u} (e_\mu \cdot e_{\lambda\alpha})^2$. The cumulative weight of all modes up to mode μ is $D_{\mu\alpha} = \sum_{i=1}^{\mu} C_{i\alpha}$. Each mode μ is then partitioned among one or more component α of one or more pseudotriplets j with weight $w_{j\mu\alpha}$ according to the following “bottom-up” filling. If $[D_{\mu\alpha}] = [D_{(\mu-1)\alpha}]$, then $w_{([D_{\mu\alpha}]+1)\mu\alpha} = C_{\mu\alpha}$. Otherwise, $w_{([D_{\mu\alpha}]+1)\mu\alpha} = D_{\mu\alpha} - [D_{\mu\alpha}]$ and $w_{[D_{\mu\alpha}]\mu\alpha} = [D_{\mu\alpha}] - D_{(\mu-1)\alpha}$. The overall weight of mode μ in pseudotriplet j is given by $w_{j\mu} = (\sum_{\alpha} w_{j\mu\alpha})/3$.

The frequencies associated with the pseudotriplets are given as follows:

$$\frac{1}{\nu_j^2} = \sum_{\mu} \frac{w_{j\mu}}{\nu_{\mu}^2}. \quad (\text{IV.1})$$

The total dielectric contribution of a pseudotriplet is

$$\kappa_j = \sum_{\mu; w_{j\mu\alpha} > 0} (w_{j\mu\alpha}/C_{\mu\alpha}) \kappa_{\mu}, \quad (\text{IV.2})$$

and the mode effective charges for the pseudotriplets are given by

$$\bar{Z}_j^* = \sqrt{V \epsilon_0 m_0 \omega_j^2 \kappa_j}. \quad (\text{IV.3})$$

The pseudotriplet averages are given in Tables VIII- IX

As can be seen by the figures, the lowest and highest pseudotriplets of CT are clearly associated with triplets in the distorted structure, as well as the two highest pseudotriplets of CAN. For the other triplets, significant mode mixing has taken place.

TABLE VIII: Phonon pseudotriplet properties for CT. ν in cm^{-1} ; \bar{Z}^* in $|e|$, B in 10^{18} J/m^4 .

ν	\bar{Z}^*	B	κ	$\% \kappa_{tot}$
98	3.36	12.38	259.99	94.6
217	1.24	1.89	7.18	2.6
509	1.30	7.14	1.44	0.5
(κ_{∞})			6.08	2.2

TABLE IX: Same as Table VIII, for CAN.

ν	\bar{Z}^*	B	κ	$\% \kappa_{tot}$
194	1.31	1.22	10.05	39.6
302	1.78	2.16	7.63	30.1
425	1.17	6.30	1.68	6.6
613	1.35	22.19	1.06	4.2
(κ_{∞})			4.93	19.4

V. ANHARMONICITY AND TEMPERATURE COEFFICIENT

In Section I, we outlined a method whereby τ_f could be determined in principle by solving the coupled anharmonic quantum oscillator problem for the system. Practical solution of this problem is difficult because the normal mode basis for the system is uncountably large: for a system with N atoms per unit cell, there are $3N$ normal modes for each wavevector \mathbf{q} in the Brillouin zone. To obtain sufficient anharmonic lattice parameters from first principles to be able to solve this problem for materials as complex as CT or CAN, would be very computationally expensive. Instead, we make a series of approximations in order to obtain a model for which we can compute all of the anharmonic terms and then solve numerically.

(1) The unit cell is kept the same at all temperatures. This allows the normal mode coordinates and expansion of total energy in normal mode coordinates to be calculated once and then used at all temperatures. This approximation is not valid near a ferroelastic where the coupling between strain and lattice dynamics is too important to ignore. In CT and, presumably CAN, ferroelastic phase transitions involving oxygen octahedra rotation do take place[32, 33]; however, the transition temperatures are far above room temperature. (2) We include only the zone-center infrared-active normal mode degrees of freedom in our model. (3) We ignore coupling between the different degrees of freedom. (4) We truncate the potential for each degree of freedom to fourth order.

Since the different degrees of freedom in the model are decoupled, the ionic susceptibility becomes a sum over modes of the susceptibility due to each mode:

$$\kappa_{\alpha\beta} = (\kappa_{\infty})_{\alpha\beta} + \frac{1}{\epsilon_0} \sum_{\mu} \frac{\partial \langle (P_{\mu})_{\alpha} \rangle}{\partial E_{\beta}}, \quad (\text{V.1})$$

where $\langle \mathbf{P}_{\mu} \rangle$ is the expectation value of the polarization of mode μ at temperature T . We have $\langle \mathbf{P}_{\mu} \rangle = \bar{\mathbf{Z}}_{\mu}^* \langle$

$\xi_\mu > /V$, where $\langle \xi_\mu \rangle$ is the expectation value of the mode amplitude ξ_μ . Furthermore, $\partial \langle \xi_\mu \rangle / \partial E_\beta = \bar{Z}_{\mu\beta}^* \partial \langle \xi_\mu \rangle / \partial \hat{E}$, where \hat{E} is a perturbation normalized so that when its value is 1, it introduces 1 J/m change in the potential. Thus

$$\kappa_{\alpha\beta} = (\kappa_\infty)_{\alpha\beta} + \sum_\mu \frac{\bar{Z}_{\mu\alpha}^* \bar{Z}_{\mu\beta}}{V\epsilon_0} \frac{\partial \langle \xi_\mu \rangle}{\partial \hat{E}}. \quad (\text{V.2})$$

For an ideal ceramic,

$$\kappa = (\kappa_\infty) + \sum_\mu \frac{1}{3} \frac{\bar{Z}_\mu^2}{V\epsilon_0} \frac{\partial \langle \xi_\mu \rangle}{\partial \hat{E}}. \quad (\text{V.3})$$

For each oscillator, the problem is that of a particle of mass m_0 in an anharmonic well. For the case of the zone-center polar modes in CT and CAN, all odd-order terms in the total energy disappear, and our expression for the total potential becomes

$$V = V_0 + \sum_\mu (A_\mu \xi_\mu^2 + B_\mu \xi_\mu^4). \quad (\text{V.4})$$

A_μ are already known from the calculation of normal mode frequencies:

$$A_\mu = \frac{1}{2} m_0 \omega_\mu^2. \quad (\text{V.5})$$

Note that in the harmonic case, $\partial \langle \xi_\mu \rangle / \partial \hat{E} = 1/(m_0 \omega_\mu^2)$ and Eqs. V.2-V.3 revert to Eqs. II.2 and II.5.

The anharmonic terms cause the permittivity to deviate from its value in the harmonic approximation. We determined B_μ by a series of first-principles frozen-phonon total energy calculations in which the each phonon, in turn, was frozen in with amplitudes $0.4n \text{ \AA}$; $n = 1$ to 4. A least-squares fit was then used to obtain B_μ . The results are shown in Tables IV-V and Figure 4. The pseudotriplet averages are given by $B_j = \sum_\mu w_{j\mu} B_\mu$. In general, the fourth-order anharmonic terms are positive and they increase as the frequency increases. The lowest-frequency modes in CT are a noteworthy exception to this trend.

To solve for $\partial \xi_\mu / \partial \hat{E}$ numerically, we used as a basis set the eigenstates of the corresponding unperturbed harmonic oscillator. The perturbations $B_\mu \xi_\mu^4$ and $\hat{E} \xi_\mu$ were written in terms of creation and annihilation operators. The eigenenergies and eigenvectors were then determined by matrix diagonalization. $\langle \xi_\mu \rangle$ were then found by writing ξ_μ in terms of creation and annihilation operators and using elementary matrix operations. By taking the limit $\hat{E} \rightarrow 0$, we computed $\partial \xi_\mu / \partial \hat{E}$ as a function of temperature for $T = 0, 5, 10, \dots, 350 \text{ K}$, and from Eq. V.3, we obtained $\kappa(T)$. Our results are shown in Figures 5-6. In Tables IV-V, we give the contribution of each mode to κ at zero temperature and at room temperature. The total τ_f at room temperature and the partial contributions of each mode to τ_f are also given, where Eq. (I.1)

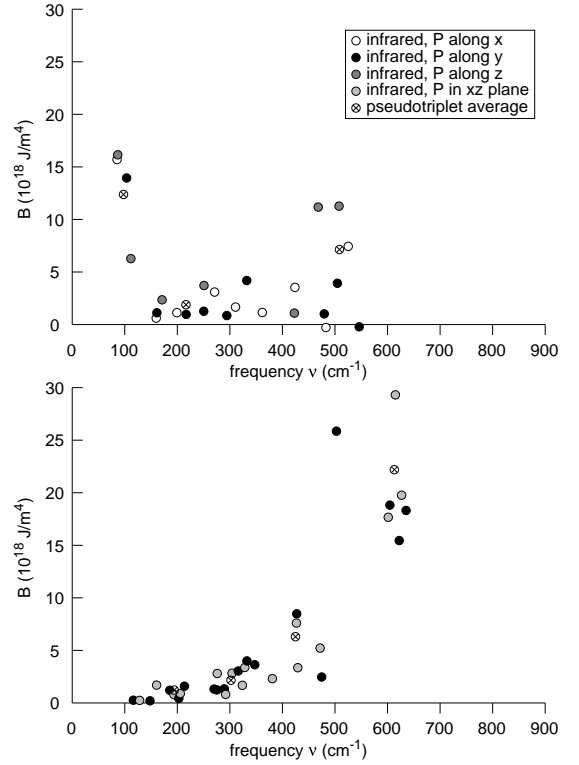


FIG. 4: Fourth order anharmonic coefficients for polar modes in CT and CAN

is used to related τ_κ to τ_f . For consistency, we set $\alpha = 0$. Experimentally, α is $11 \times 10^{-6} \text{ K}^{-1}$ for CT[34]; assuming a similar value for α in CAN, τ_f is dominated by the $-\tau_\kappa/2$ contribution in both cases.

VI. DISCUSSION

In the harmonic approximation, we find $\kappa = 276.0$ for CT and $\kappa = 25.3$ for CAN. The CT values compares well with the experimental room temperature values of 170 and the CAN value is in very good agreement with the room temperature value of 27. The harmonic approximation should hold best at low temperatures. Experimentally, $\kappa \approx 330$ [9] for CT at $T = 0$. Extrapolating the room-temperature results for CAN to $T = 0$ using the experimental τ_ϵ value at room temperature, the low temperature permittivity of CAN is about 23. The agreement with the zero temperature experimental results is very good. The computed individual components of the permittivity tensor for CAN are $\kappa_{xx} = 24.08$, $\kappa_{yy} = 24.32$, $\kappa_{zz} = 27.63$, and $\kappa_{xz} = 0.19 + (\kappa_\infty)_{xz}$. Assuming that $(\kappa_\infty)_{xz}$ is small, the principal axes of the dielectric tensor are close to the Cartesian axes. The predicted anisotropy in the single crystal dielectric properties of CAN is less than that for CT[13].

In each case, polar pseudotriplet analysis shows that the lowest pseudotriplet contributes the most to the per-

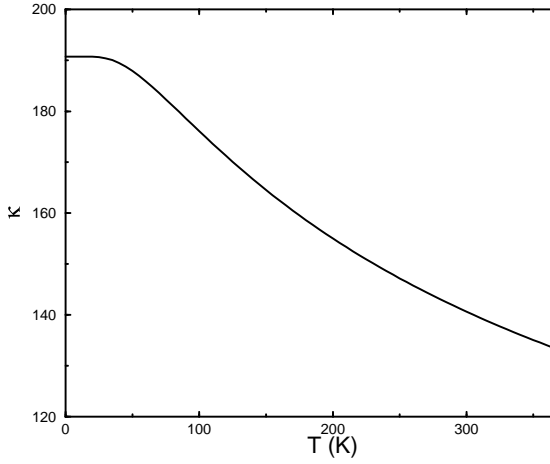


FIG. 5: Temperature dependence of permittivity in CT in independent anharmonic oscillator model.

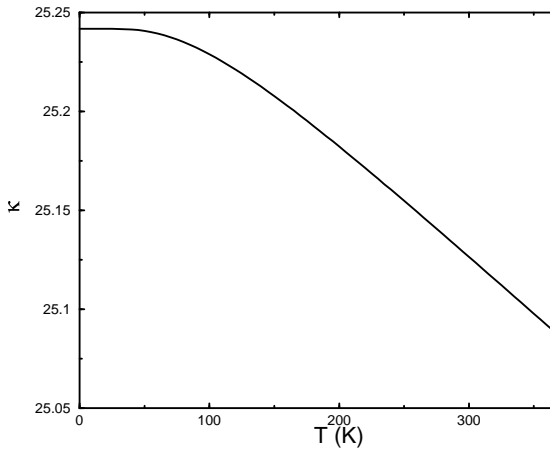


FIG. 6: Temperature dependence of permittivity in CAN in independent anharmonic oscillator model.

mittivity (see Tables VIII-IX). In CT, this pseudotriplet dominates the permittivity, contributing nearly 95% of the total, while in CAN, the lowest frequency pseudotriplet only contributes about 40 % of the permittivity. In CAN, the contributions of second pseudotriplet and the electronic permittivity are relatively important.

In each case, $\kappa \approx 15 + \kappa_{pt1}$, where κ_{pt1} is the contribution of the lowest frequency pseudotriplet. The decrease in κ_{pt1} between CT and CAN is due to several factors. In the following thought experiment, we see how each of the factors affects κ_{pt1} . First, we decrease the individual ionic effective charges from their values in CT to their values in CAN. κ_{pt1} decreases from 260 to 157 due to the lower ionic Born effective charges in CAN. Next, we raise the pseudotriplet frequency from its value in CT to its value in CAN. κ_{pt1} decreases further to 40. Finally, we change the eigenvectors of the low-frequency modes to those of CAN. κ_{pt1} drops to its value of 10 in CAN.

The change in pseudotriplet frequency and change in

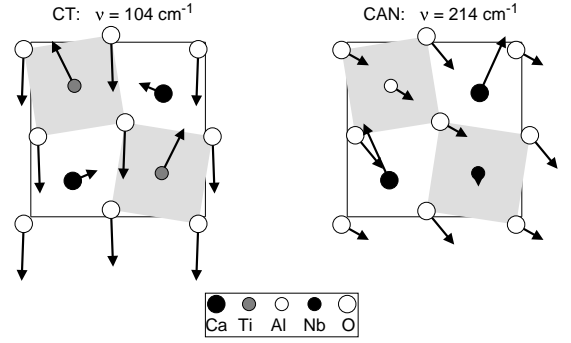


FIG. 7: Comparison of eigenvectors of representative low frequency modes in CT and CAN. A cross section is projected onto the xy plane. Cross sections of BO_6 octahedra are shaded in gray

pseudotriplet eigenvectors are the most significant factors in explaining the different permittivities of CT and CAN and are equally important. How does the difference in the eigenvectors lead to a lower effective charge in CAN? In Figure 7, we show the eigenvectors of comparable representative low-frequency polar phonons in the two cases, both with frequencies and effective charges close to the corresponding pseudotriplet average, and both with net polarization in the \hat{y} direction. In CT, all cations move in the same direction as the anions, leading to a large \overline{Z}^* via Eq. (II.3). In CAN, the Ca and the O again move in opposite directions, but now the Al and Nb move in the same direction as the O. Positive and negative charges moving in the same direction lowers \overline{Z}^* and reduces permittivity.

In Table IV, we see that anharmonic terms lead to significant changes in permittivity of CT relative to its value in the harmonic approximation, even at zero temperature (due to quantum zero point motion). Furthermore, they lead to significant temperature dependence of κ . The qualitative variation of κ in CT with temperature shows excellent agreement with experiment, decreasing monotonically, and having an inflection point at $T \approx 100$ K. In CAN, similar effects are predicted, but with much smaller magnitude. The predicted room temperature permittivities for this model are 180 for CT and 25 for CAN, in very good agreement with experiment.

Our model gives $\tau_f = +428 \times 10^{-6} \text{ K}^{-1}$ in CT and $\tau_f = +11 \times 10^{-6} \text{ K}^{-1}$ in CAN. Since the system is modelled as decoupled oscillators, we see the contribution of individual modes to τ_f . In both CT and CAN, the lowest frequency polar modes dominate τ_f . The agreement with the experimental values of $+900 \times 10^{-6} \text{ K}^{-1}$ and $-88 \times 10^{-6} \text{ K}^{-1}$, respectively, is only fair. This is due both to LDA errors and to the approximations used in the models. The model fails to incorporate coupling between different modes and the coupling of the lattice dynamics to strain (*i.e.* thermal expansion). In particular, the coupling of the low frequency optical modes

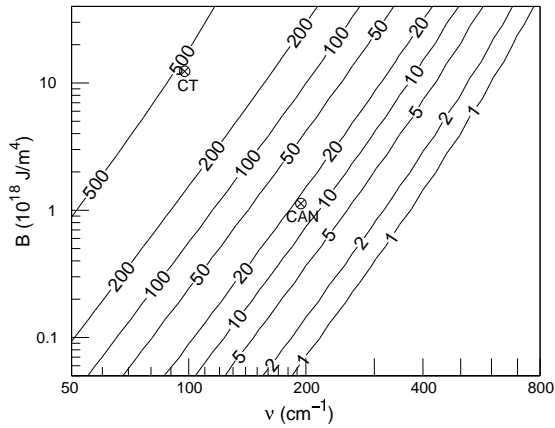


FIG. 8: τ_f (in 10^{-6} K^1) for a system with a single polar triplet of frequency ν and quartic anharmonic coefficient B , assuming no thermal expansion and no coupling of the triplet to other modes or strain.

to the acoustic branch has been found to be important in the temperature-dependent lattice dynamics of perovskite oxides such as KNbO_3 [35], and should therefore have an important quantitative effect on $\kappa(T)$.

Nonetheless, the simple model presented here reproduces qualitatively the difference between the τ_f of CT and CAN and thus shows that the model captures a significant piece of physics: namely, anharmonicity within low-frequency polar phonons with a positive fourth order coefficient tends to lead to a positive τ_f . In the context of a decoupled oscillator model, we can see the relative effect of frequency and anharmonicity of a mode on τ_f . We assume that $\kappa \gg \kappa_\infty$ and that the system is cubic and has one triply degenerate set of polar modes. The computed τ_f for this case is shown in Figure 8. For comparison, the lowest pseudotriplet properties for CT and CAN are shown. It can be seen that both the lower frequency and the higher positive anharmonicity of the low-frequency polar phonons in CT lead to its much more positive τ_f .

Why is the anharmonicity of the low-frequency polar modes in CT so high? It is a consequence of the eigenvectors of the low-frequency phonons. In CT, the Ti inside the BO_6 octahedron move against the oxygens. At relatively low amplitude, the short-range repulsion between Ti and O becomes significant, leading to an increase in the potential and thus a large positive B . In CAN, on the other hand, both Al and Nb move roughly in tandem with the surrounding O octahedra. The low-frequency modes can thus go to significantly larger amplitude before the effects of short range repulsion becomes significant and thus B is lower. We thus conclude that the same factors (lower frequency and type of eigenvector) that give CT a much higher permittivity than CAN give it a τ_f that is more positive and larger in magnitude.

We see from Figure 8 that to simultaneously obtain very high permittivity (which requires low- ν modes) and

τ_f near zero would require either exceptionally low anharmonicity or else for couplings not included in the model to counteract the tendency[36, 37] of high- κ materials to have large positive τ_f .

The difference in eigenvector between CT and CAN is significant. Why do B site cations move against the O octahedra in CT and not in CAN? We first note that in the case of simple perovskites involving Nb, such as KNbO_3 (KN), Nb moves against the oxygens in the lowest frequency polar modes[27, 38]. This difference in the behavior of Nb in KN and CAN is not due to size effects: the Nb-O distances in the two compounds are almost identical. We look instead at the difference in electronic structure.

It is well known that hybridization of oxygen 2p electrons with B site transition metal d electrons is important for ferroelectricity and incipient ferroelectricity[39, 40]. In the case of SrTiO_3 vs. SrHfO_3 , Stachiotti *et al.*[41] showed a difference between the eigenvectors of the lowest frequency polar modes very analogous to the differences between CT and CAN: in SrTiO_3 , the Ti tends to move against the oxygens; in SrHfO_3 , the Hf tends to move with the oxygens. They conclude that Ti 3d- O 2p covalency in SrTiO_3 is more important than Hf 5d- O 2p covalency in SrHfO_3 .

One expects an inverse relationship between the importance of covalent bonding in a perovskite and the band gap, all other factors being the same. Indeed, the band gap in SrHfO_3 is larger than in SrTiO_3 [42]. With this in mind, we calculated the band gaps in CT, CAN, and KN. Although density functional theory does not correctly give the magnitudes of band gaps[43], we expect the relative differences to hold. Our results are shown in Table X.

TABLE X: LDA band gaps and nature of lowest conduction state in CT, CAN, and KN.

Compound	Band gap	Dominant atomic contribution to lowest conduction state
CaTiO_3	1.91 eV	Ti 3d
$\text{CaAl}_{1/2}\text{Nb}_{1/2}\text{O}_3$	2.76 eV	Nb 4d
KNbO_3	1.39 eV	Nb 4d

Our results support the hypothesis that larger band gaps lead to lesser importance of covalent bonding and less tendency of B site cations to move against the oxygens in the low-frequency phonons. The reason for the larger gap in CAN than KN is due to the presence of the Al. The Al ions contribute no low-lying energy levels to the conduction bands. The lowest-lying conduction states come mainly from Nb-4d electrons. In a simple perovskite with Nb on every B site, the lowest conduction state wavefunction is spread over all the B sites and is more plane-wave-like than in a complex perovskite where Nb and thus the wavefunction is distributed on only half the sites. The more localized wavefunctions in the complex perovskite lead to higher eigenenergies and thus a

larger band gap. It would be interesting to see how the type and ordering of the B site cations affects the electronic structure, phonon behavior, and dielectric properties of complex perovskites in general.

VII. CONCLUSIONS

We have used first-principles computations and compare the dielectric properties of CaTiO_3 and $\text{CaAl}_{1/2}\text{Nb}_{1/2}\text{O}_3$. The difference in relative permittivity is largely due to differences in the low-frequency polar phonons in the two systems. In CAN, these phonons have higher frequency and qualitatively different phonon eigenvectors than in CT, therefore suppressing the permittivity. We introduce and solve a model for the temperature dependence of dielectric constant and thus τ_f . The differences in τ_f for the two systems are again correlated with the differences in the properties of the low frequency phonons. Our results demonstrate that the details of B-site cation chemistry in complex perovskites has an effect on the lattice dynamics and dielectric properties not wholly accounted for by size effects.

VIII. ACKNOWLEDGEMENTS

I thank B.P. Burton, J. Y. Chan, I. Levin for useful discussions and T. A. Vanderah for suggesting this study. I thank G. Kresse for making VASP version 4.4.4 available to us. This work was supported by the National Research Council.

REFERENCES

- [1] R. D. Shannon, *J. Appl. Phys.* **73**, 348 (1993).
- [2] E. L. Colla, I. M. Reaney, and N. Setter, *Ferroelectrics* **133**, 217 (1992).
- [3] E. L. Colla, I. M. Reaney, and N. Setter, *J. Appl. Phys.* **74**, 3414 (1993).
- [4] V. Sivasubramanian, V. R. K. Murthy, and B. Viswanathan, *Jpn. J. Appl. Phys.* **36**, 194 (1997).
- [5] C.-I. Cheon and J.-S. Kim, *J. Mater. Res.* **13**, 1107 (1998).
- [6] M. Valant, D. Suvarov, and C. J. Rawn, *Jpn. J. Appl. Phys. Part I* **38**, 2820 (1999).
- [7] I. Levin, J. Y. Chan, T. A. Vanderah, J. E. Maslar, and S. M. Bell, unpublished.
- [8] G. Rupprecht and R. O. Bell, *Phys. Rev.* **135**, A748 (1964).
- [9] V. V. Lemanov, A. V. Sotnikov, E. P. Smirnova, M. Weihnacht, and R. Kunze, *Solid State Comm.* **110**, 611 (1999).
- [10] R. C. Kell, A. C. Greenhaum, and G. C. E. Olds, *J. Am. Ceram. Soc.* **56**, 352 (1973).
- [11] H. Kagata and J. Kato, *Jpn. J. Appl. Phys.* **33**, 5463 (1994).
- [12] T. A. Vanderah, W. Febo, J. Y. Chan, R. S. Roth, J. M. Loezos, L. D. Rotter, R. G. Geyer, and D. B. Minor, *J. Solid State Chem.* **155**, 78 (2000).
- [13] E. Cockayne and B. P. Burton, *Phys. Rev. B* **62**, 3735 (2000).
- [14] M. Born and K. Huang, "Dynamical Theory of Crystal Lattices" (Oxford: Oxford University Press), 1954.
- [15] Ph. Ghosez, X. Gonze, and J.-P. Michenaud, *Ferroelectrics* **194**, 39 (1997).
- [16] G. Kresse and J. Hafner, *Phys. Rev. B* **47**, RC558 (1993).
- [17] G. Kresse, Thesis, Technische Universität Wien, 1993.
- [18] G. Kresse and J. Furthmüller, *Comput. Mat. Sci.* **6**, 15 (1996).
- [19] G. Kresse and J. Furthmüller, *Phys. Rev. B* **54**, 11169 (1996).
- [20] D. Vanderbilt, *Phys. Rev. B* **41**, 7892 (1990).
- [21] G. Kresse and J. Hafner, *J. Phys.: Condens. Matter* **6**, 8245 (1994).
- [22] R. E. Cohen and H. Krakauer, *Ferroelectrics* **136**, 65 (1992).
- [23] A. R. Chakhmouradian and R. H. Mitchell, *J. Solid State Chem.* **138**, 272 (1998).
- [24] The lattice parameters reported in Reference [12] differ slightly from the preliminary results used here.
- [25] R. D. King-Smith and D. Vanderbilt, *Phys. Rev. B* **47**, 1651 (1992).
- [26] R. Resta, M. Posternak, and A. Baldereschi, *Phys. Rev. Lett.* **70**, 1010 (1993).
- [27] C.-Z. Wang, R. Yu, and H. Krakauer, *Phys. Rev. B* **54**, 11161 (1996).
- [28] L. Bellaiche, J. Padilla, and D. Vanderbilt, *Phys. Rev. B* **59**, 1834 (1999).
- [29] F. Bernardini, V. Fiorentini, and D. Vanderbilt, *Phys. Rev. Lett.* **79**, 3958 (1997).
- [30] F. Bernardini and V. Fiorentini, *Phys. Rev. B* **58**, 15292 (1998).
- [31] In order to calculate phonon frequencies with respect to an equilibrium structure, the structure was first relaxed while maintaining cubic symmetry, upon which each O moved 0.061 Å away from the closest Nb toward the closest Al.
- [32] T. Matsui, H. Shigematsu, Y. Arita, Y. Hanajiri, N. Nakamitsu, and T. Nagasaki, *J. Nucl. Mater.* **247**, 72 (1997).
- [33] B. J. Kennedy, C. J. Howard, and B. C. Chakoumakos, *J. Phys.: Condens. Matter* **11**, 1479 (1999).
- [34] S. A. T. Redfern, *J. Phys: Condens. Matter* **8**, 8267 (1996).
- [35] M. Holma and H. Chen, *J. Phys. Chem. Solids* **57**, 1465 (1996).
- [36] A. J. Bosman and E. E. Havinga, *Phys. Rev.* **129**, 1593 (1963).

- [37] A. G. Cockbain and P. J. Harrop, *Brit. J. Appl. Phys. (J. Phys. D.)* ser. 2 **1**, 1109 (1968).
- [38] A. V. Postnikov, T. Neumann and G. Borstel, *Ferroelectrics* **164**, 101 (1995).
- [39] R. E. Cohen, *Nature* **358**, 136 (1992).
- [40] M. Posternak, R. Resta, and A. Baldereschi, *Phys Rev. B* **50**, 8911 (1994).
- [41] M. G. Stachiotti, G. Fabricius, R. Alonso, and C. O. Rodriguez, *Phys. Rev. B* **58**, 8145 (1998).
- [42] G. Fabricius, E. L. Peltzer y Blanca, C. O. Rodriguez, A. P. Ayala, P. de la Presa, and A. Lopez García, *Phys. Rev. B* **55**, 164 (1997).
- [43] R. W. Godby, M. Schlüter, and L. J. Sham, *Phys. Rev. B* **37**, 10159 (1988).